



Self-assembling supramolecular dendrimer nanosystem for PET imaging of tumors

Philippe Garrigue^{a,b}, Jingjie Tang^c, Ling Ding^c, Ahlem Bouhlel^{a,b}, Aura Tintaru^d, Erik Laurini^e, Yuanyu Huang^{f,g,h}, Zhenbin Lyu^c, Mengjie Zhang^{f,g}, Samantha Fernandez^b, Laure Balasse^{a,b}, Wenjun Lanⁱ, Eric Masⁱ, Domenico Marson^e, Yuhua Weng^{f,g}, Xiaoxuan Liu^c, Suzanne Giorgio^c, Juan Iovannaⁱ, Sabrina Pricl^e, Benjamin Guillet^{a,b}, and Ling Peng^{c,1}

^aAix-Marseille University, INSERM, INRA, Center de Recherche en Cardiovasculaire et Nutrition (C2VN), 13385 Marseille, France; ^bAix-Marseille University, Centre Européen de Recherche en Imagerie Médicale (CERIMED), 13005 Marseille, France; ^cAix-Marseille University, CNRS, Centre Interdisciplinaire de Nanoscience de Marseille (CINaM), Equipe Labellisée Ligue Contre le Cancer, 13288 Marseille, France; ^dAix-Marseille University, CNRS, Institut de Chimie Radicale (ICR), 13013 Marseille, France; ^eMolecular Biology and Nanotechnology Laboratory, Department of Engineering and Architecture, University of Trieste, 34127 Trieste, Italy; ^fAdvanced Research Institute of Multidisciplinary Science, Beijing Institute of Technology, Beijing 100081, China; ^gSchool of Life Science, Beijing Institute of Technology, Beijing 100081, China; ^hSchool of Pharmacy, Hunan University of Chinese Medicine, Changsha 410208, China; and ⁱAix-Marseille University, CNRS, INSERM, Institut Paoli-Calmettes, Centre de Recherche en Cancérologie de Marseille (CRCM), 13273 Marseille, France

Edited by Michael L. Klein, Temple University, Philadelphia, PA, and approved September 26, 2018 (received for review July 27, 2018)

Bioimaging plays an important role in cancer diagnosis and treatment. However, imaging sensitivity and specificity still constitute key challenges. Nanotechnology-based imaging is particularly promising for overcoming these limitations because nanosized imaging agents can specifically home in on tumors via the “enhanced permeation and retention” (EPR) effect, thus resulting in enhanced imaging sensitivity and specificity. Here, we report an original nanosystem for positron emission tomography (PET) imaging based on an amphiphilic dendrimer, which bears multiple PET reporting units at the terminals. This dendrimer is able to self-assemble into small and uniform nanomicelles, which accumulate in tumors for effective PET imaging. Benefiting from the combined dendrimeric multivalence and EPR-mediated passive tumor targeting, this nanosystem demonstrates superior imaging sensitivity and specificity, with up to 14-fold increased PET signal ratios compared with the clinical gold reference 2-fluorodeoxyglucose (¹⁸F]FDG). Most importantly, this dendrimer system can detect imaging-refractory low-glucose-uptake tumors that are otherwise undetectable using ¹⁸F]FDG. In addition, it is endowed with an excellent safety profile and favorable pharmacokinetics for PET imaging. Consequently, this dendrimer nanosystem constitutes an effective and promising approach for cancer imaging. Our study also demonstrates that nanotechnology based on self-assembling dendrimers provides a fresh perspective for biomedical imaging and cancer diagnosis.

dendrimer | supramolecular nanomicelle | bioimaging | EPR effect | tumor diagnosis

Early and precise diagnosis constitutes an essential step for successful management of many diseases, and for cancer in particular. Although the advancement of molecular imaging has greatly improved cancer detection and diagnosis, tumor imaging using noninvasive techniques still faces problems relating to detection sensitivity, spatial resolution, and depth penetration, which affect the imaging quality and accuracy. Application of nanotechnology to the specific delivery of imaging agents to tumor lesions is widely expected to overcome these limitations and bring breakthroughs in cancer imaging and diagnosis (1, 2). This is because nanosized agents can specifically enter into and accumulate within tumor lesions via the “enhanced permeation and retention” (EPR) effect thanks to the leaky vasculature and dysfunctional lymphatic drainage in the tumor microenvironment (3–5). The EPR effect—also referred to as passive tumor targeting—can potentially boost the local concentration of the imaging agent in tumors, thereby improving imaging sensitivity and resolution (1, 2).

Self-assembly is a very powerful approach to create nanosystems in a modular and specific way, yet with relatively little synthetic effort (6). Recently, self-assembled supramolecular

nanostructures formed from amphiphilic dendrimers (7–9) have emerged as innovative and effective drug delivery systems. These amphiphilic dendrimers couple the self-assembling feature of lipids with the well-defined dendritic structure and stability of dendrimers to generate nanocarriers with appropriate sizes, tailored properties, and high drug loading (8, 10, 11). For imaging, we reasoned that the dendritic multivalency of these specific amphiphiles could offer, upon conjugation, the unique capacity of carrying abundant copies of the contrast or imaging agents, ultimately resulting in better and more precise imaging. Accordingly, in this proof-of-concept study, we report a self-assembling amphiphilic dendrimer nanosystem that combines EPR-mediated tumor accumulation with the multivalent feature of dendrimer for effective tumor imaging using positron emission tomography (PET) (Fig. 1).

PET imaging is, among various noninvasive functional imaging modalities, commonly used in nuclear medicine to assess pathophysiological functions. It has gained wide acceptance in

Significance

Nanotechnology-based imaging is expected to bring breakthroughs in cancer diagnosis by improving imaging sensitivity and specificity while reducing toxicity. Here, we developed an innovative nanosystem for positron emission tomography (PET) imaging based on a self-assembling amphiphilic dendrimer. This dendrimer assembled spontaneously into uniform supramolecular nanomicelles with abundant PET reporting units on the surface. By harnessing both dendrimeric multivalence and the “enhanced permeation and retention” (EPR) effect, this dendrimer nanosystem effectively accumulated in tumors, leading to exceedingly sensitive and specific imaging of various tumors, especially those that are otherwise undetectable using the clinical gold reference 2-fluorodeoxyglucose (¹⁸F]FDG). This study illustrates the power of nanotechnology based on self-assembling dendrimers to provide an effective platform for bioimaging and related biomedical applications.

Author contributions: P.G., Y.H., J.L., S.P., B.G., and L.P. designed research; P.G., J.T., L.D., A.B., A.T., E.L., Z.L., M.Z., S.F., L.B., W.L., E.M., D.M., and S.G. performed research; J.T. and A.B. contributed new reagents/analytic tools; P.G., J.T., L.D., A.B., A.T., E.L., Y.H., Y.W., X.L., S.G., S.P., B.G., and L.P. analyzed data; and P.G., S.P., B.G., and L.P. wrote the paper.

The authors declare no conflict of interest.

This article is a PNAS Direct Submission.

This open access article is distributed under [Creative Commons Attribution-NonCommercial-NoDerivatives License 4.0 \(CC BY-NC-ND\)](https://creativecommons.org/licenses/by-nc-nd/4.0/).

¹To whom correspondence should be addressed. Email: ling.peng@univ-amu.fr.

This article contains supporting information online at www.pnas.org/lookup/suppl/doi:10.1073/pnas.1812938115/-DCSupplemental.

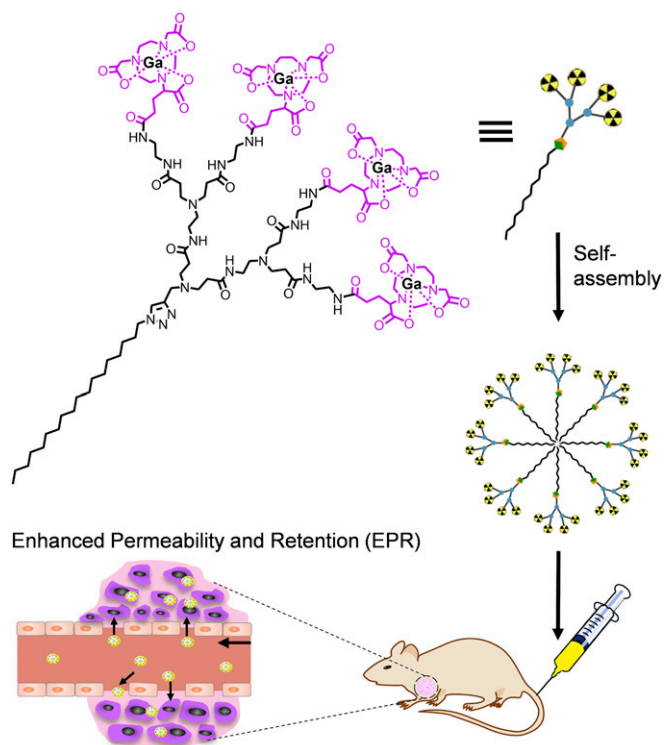


Fig. 1. Schematic illustration of the supramolecular dendrimer nanosystem, based on a self-assembling amphiphilic dendrimer bearing radionuclide terminals, for positron emission tomography (PET) imaging of tumors.

oncologic imaging mainly because of its excellent sensitivity up to the femtomolar range, with quantitative imaging capabilities and limitless depth of penetration (12, 13). Moreover, hybrid cameras enable precise anatomic localization of PET functional

imaging via coregistration with X-ray computed tomography (CT) (14). In this study, we selected gallium-68 [^{68}Ga] as the high-energy positron-emitter radioisotope because it is an interesting and common PET radiotracer with a physical half-life of 68 min, a time long enough for imaging acquisition yet short enough for safe radioprotection of both patients and medical staff (15). In addition, generation of clinically used radioactive $^{68}\text{Ga}(\text{III})$ can be conveniently achieved using homemade facilities for on-demand production via a $^{68}\text{Ge}/^{68}\text{Ga}$ generator. It should be noted that a chelator is required to enable stable $^{68}\text{Ga}(\text{III})$ radiolabeling for PET imaging (16). We therefore opted for 1,4,7-triazacyclononane-1,4,7-triacetic acid (NOTA) as the Ga(III) chelator because of its advantages over the commonly used 1,4,7,10-tetraazacyclododecane-1,4,7,10-tetraacetic acid (DOTA). In fact, NOTA chelates Ga(III) with superior thermodynamic stability and kinetic inertness (17) than DOTA, thanks to the perfect match of size, geometry, and denticity between the NOTA macrocycle and the small radionuclide Ga(III). This, in turn, is reflected in favorable enthalpic and entropic contributions to the chelation (18). Also, NOTA is able to complex Ga(III) rapidly and efficiently at room temperature and has high stability in vivo (16, 19). Given the large size of the NOTA macrocycle, to avoid eventual synthetic difficulty (20–22) and instability stemming from possible steric congestion of the dendrimer terminals, we chose to focus on the lowest generation amphiphilic dendrimer **1**, which bears four NOTA terminals and one hydrophobic alkyl chain (Fig. 1). This small amphiphilic dendrimer can indeed self-assemble into stable and uniform nanomicelles, which effectively accumulate in tumors via the EPR effect, leading to specific and sensitive imaging of tumors. Most importantly, this dendrimer nanosystem is able to detect, with exceedingly high signal-to-noise ratios, the imaging-refractory low-glucose-uptake tumors that are otherwise difficult to image using the clinical gold reference 2-fluorodeoxyglucose (^{18}F)FDG). This original supramolecular imaging system based on self-assembling amphiphilic dendrimer therefore constitutes a promising nanoplatform for cancer imaging and detection.

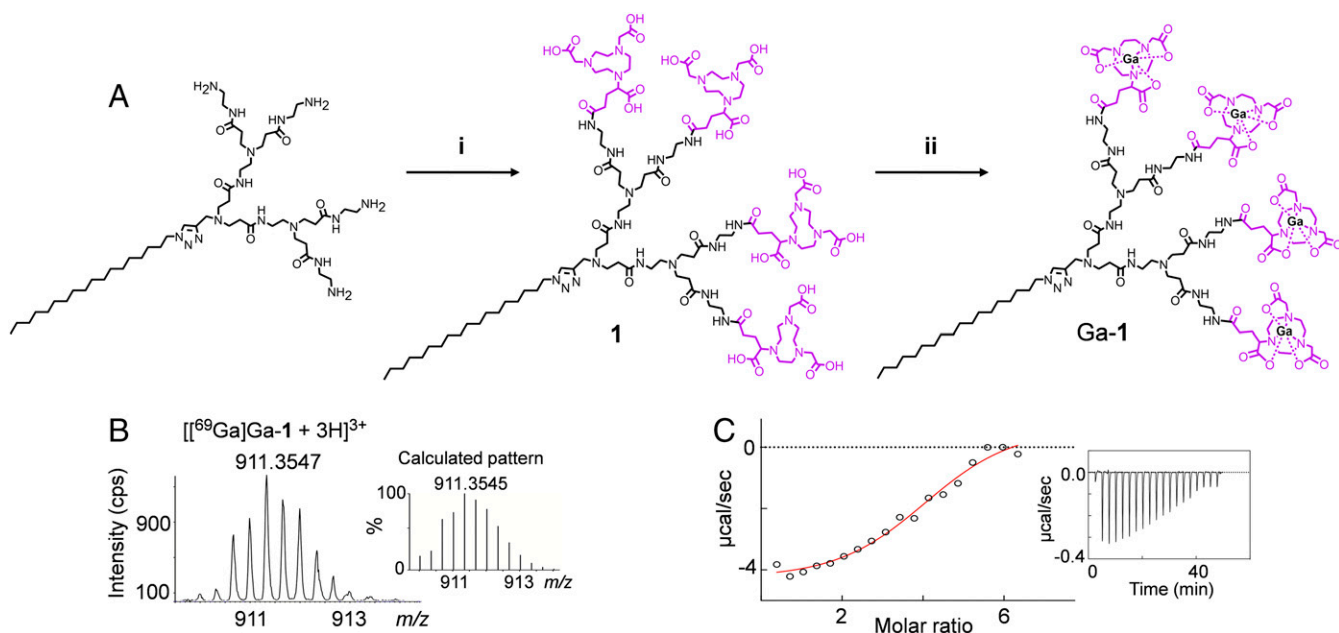


Fig. 2. Synthesis of the amphiphilic dendrimer **1** and its chelation with the nonradioactive isotope $^{69}\text{GaGa}^{3+}$ at the terminals. (A) Synthesis scheme: (i) (a) NODA-GA(*t*Bu) $_3$, PyBOP, NMM, DMF, 30 °C, 72 h; (b) TFA, CH_2Cl_2 , 30 °C, 16 h. (ii) $^{69}\text{GaGaCl}_3$, 1.0 M HCl, 20 °C, 15 min. (B) High-resolution mass spectrum showing the isotopic pattern characteristic of the triply charged species $^{69}\text{GaGa-1+3H}^{3+}$. The *Inset* shows the calculated isotopic pattern. (C) Isothermal titration calorimetry (ITC) curve for chelation of Ga^{3+} with dendrimer **1**. The *Inset* shows measured heat power versus time elapsed during titration.

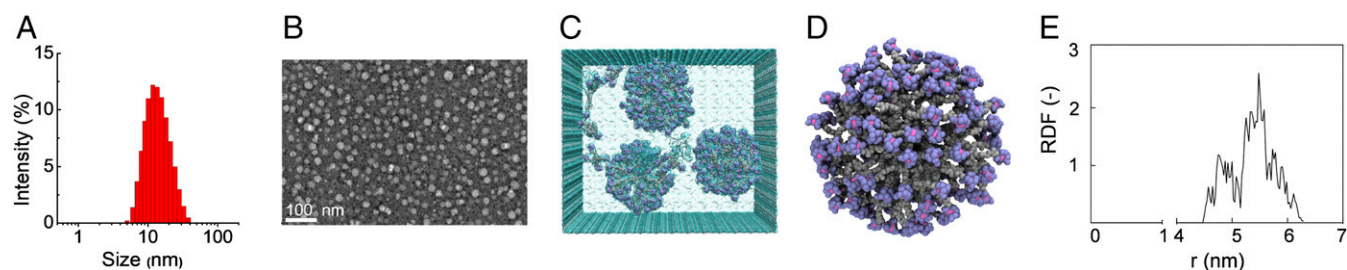


Fig. 3. Self-assembly of the amphiphilic dendrimer $[^{69}\text{Ga}]\text{Ga-1}$ into small and uniform nanomicelles. (A) Dynamic light scattering (DLS) measurement, (B) transmission electron microscopy (TEM) image, and (C–E) computer modeling of the self-assembled nanostructures formed by $[^{69}\text{Ga}]\text{Ga-1}$. (C) Final image of the $[^{69}\text{Ga}]\text{Ga-1}$ self-assembly process into spherical micelles as obtained from atomistic molecular-dynamics (MD) simulations. Different parts of the $[^{69}\text{Ga}]\text{Ga-1}$ molecules are represented as spheres (atom color: gray, hydrocarbon chain; lavender, NOTA cage; hot pink, Ga^{3+}), while water molecules are shown as aqua transparent spheres. The first water shell surrounding each molecule/micelle is highlighted as a dark aqua transparent contour. (D) Zoomed image of a $[^{69}\text{Ga}]\text{Ga-1}$ micelle as extracted from the equilibrated portion of the MD trajectory. Colors as in C. Water molecules are not shown for clarity. (E) Radial distribution function of the Ga(III)-bearing terminals as a function of the distance from the center of mass of the $[^{69}\text{Ga}]\text{Ga-1}$ micelles.

Results and Discussion

Amphiphilic Dendrimer 1 Bearing NOTA Terminals Is Able to Complex with Ga(III) and Self-Assemble into Small and Uniform Nanomicelles.

The NOTA-bearing dendrimer **1** devised for PET imaging in this work was synthesized starting with the amine-terminated amphiphilic dendrimer, which was conjugated with the reagent NODA-GA(*t*Bu)₃, followed by subsequent deprotection. The dendrimer **1** was obtained with an excellent overall yield of 83% (Fig. 2A and *SI Appendix, Scheme S1B*), and its chemical structure was confirmed using ¹H, ¹³C, and 2D NMR and high-resolution mass spectrometry (HRMS), which revealed the characteristic signals corresponding to the chemically conjugated NOTA entities (*SI Appendix, Figs. S1 and S2A*). The characteristic signals for NOTA moieties in **1** could not be observed

when simply mixing the amine-terminating dendrimer with the NOTA reagent in the absence of the coupling agent. This indicates the successful covalent conjugation of the NOTA functionality on the dendrimer terminals. Chelation of the isotope $^{69}\text{Ga}^{3+}$ by **1** using $^{69}\text{GaCl}_3$ (Fig. 2A and *SI Appendix, Scheme S1B*), followed by dialysis to remove free $^{69}\text{Ga}^{3+}$, yielded the non-radioactive dendrimer $[^{69}\text{Ga}]\text{Ga-1}$. HRMS showed the isotopic pattern characteristic of the triply charged species $[[^{69}\text{Ga}]\text{Ga-1}+3\text{H}]^{3+}$ in addition to the molecular weight peak (Fig. 2B and *SI Appendix, Fig. S2B*), confirming the successful complexation of four $^{69}\text{Ga}(\text{III})$ ions within the dendrimer **1**. Since $^{69}\text{Ga}^{3+}$ possesses a quadrupolar moment and very low NMR sensitivity (23), well-resolved NMR spectra for $[^{69}\text{Ga}]\text{Ga-1}$ could not be obtained. We therefore further studied $[^{69}\text{Ga}]\text{Ga-1}$ using isothermal titration

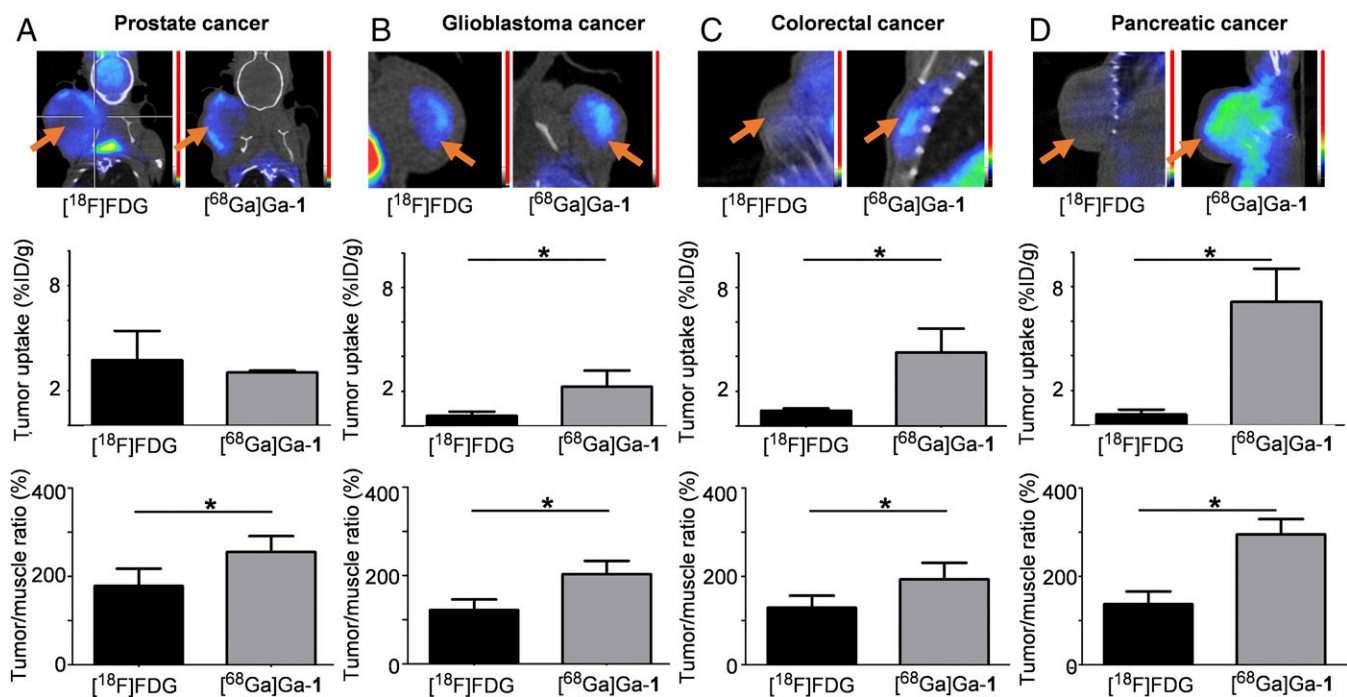


Fig. 4. Radiolabeled dendrimer $[^{68}\text{Ga}]\text{Ga-1}$ for PET imaging of various tumors. Tumor targeting and uptake assessment of $[^{68}\text{Ga}]\text{Ga-1}$ in mouse ectopic xenograft models of (A) prostate adenocarcinoma (22Rv1 cell line), (B) glioma (U87 cell line), (C) colorectal adenocarcinoma (HT-29 cell line), and (D) pancreatic adenocarcinoma (SOJ-6 cell line), in comparison with $[^{18}\text{F}]\text{FDG}$, the clinical gold reference for PET imaging in oncology. (Top) Representative examples of PET images. The orange arrows indicate tumor positions. (Middle) Quantifications from PET images of tumor uptake expressed as mean \pm SD percentage injected dose per gram ($n = 3$; except for 22Rv1, $n = 4$; $*P \leq 0.05$, Kruskal–Wallis test). (Bottom) Quantifications from PET images of tumor-to-background ratios (right forelimb biceps muscle taken as background reference). All data were expressed as mean \pm SD percentage ($n = 3$; $*P \leq 0.05$, Kruskal–Wallis test).

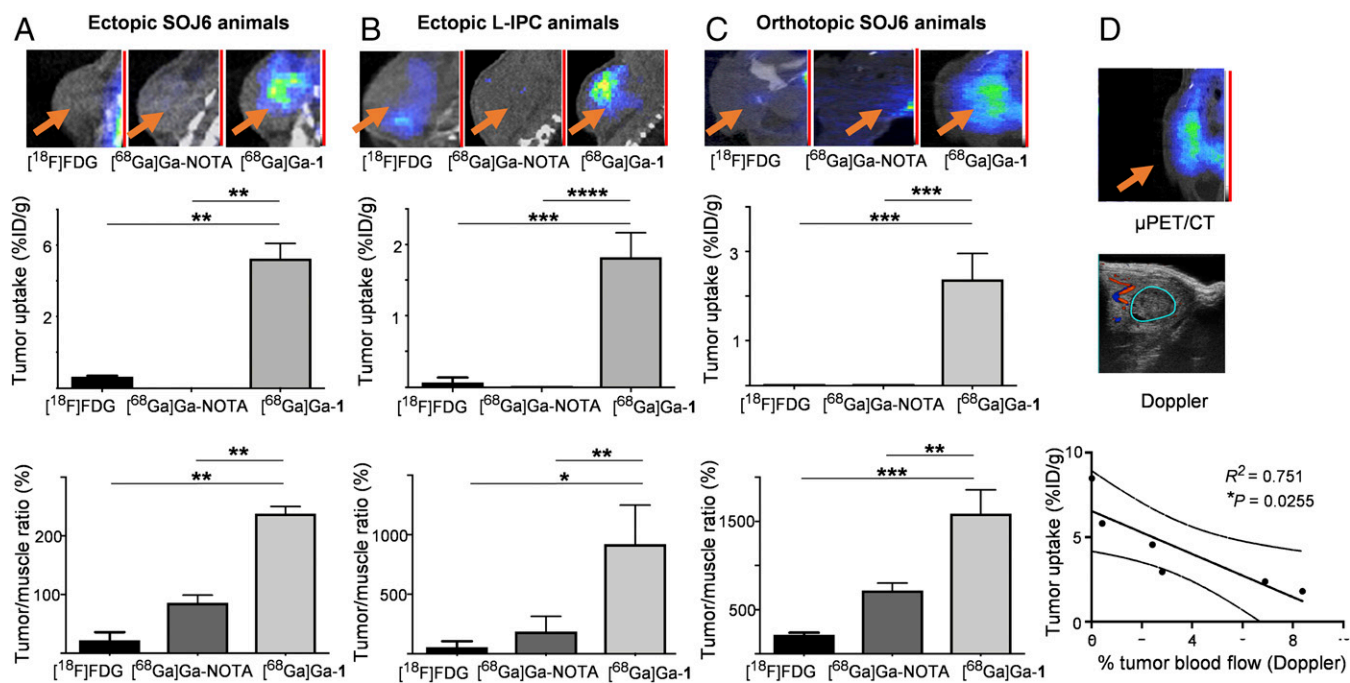


Fig. 5. EPR-based tumor uptake of $[^{68}\text{Ga}]\text{Ga-1}$ for effective PET imaging. Comparison of the tumor accumulation of the dendrimer nanosystem $[^{68}\text{Ga}]\text{Ga-1}$, the small molecular complex $[^{68}\text{Ga}]\text{Ga-NOTA}$, and the clinical reference $[^{18}\text{F}]\text{FDG}$ in ectopic (A) SOJ6- and (B) LIPC-xenografted mice as well as in (C) orthotopic SOJ6-xenograft mice. (Top) Representative examples of $[^{18}\text{F}]\text{FDG}$ (Left), $[^{68}\text{Ga}]\text{Ga-NOTA}$ (Middle), and $[^{68}\text{Ga}]\text{Ga-1}$ (Right) PET images. The orange arrows indicate tumor positions. (Middle) Quantifications from PET images of tumor uptake, expressed as mean \pm SD percentage injected dose per gram ($n = 3$; $*P \leq 0.05$, $**P \leq 0.01$, $***P \leq 0.001$, and $****P \leq 0.0001$, Kruskal–Wallis test). (Bottom) Quantifications from PET images of tumor-to-background ratios (right forelimb biceps muscle taken as background reference), expressed as mean \pm SD percentage ($n = 3$; $*P \leq 0.05$, $**P \leq 0.01$, $***P \leq 0.001$, Kruskal–Wallis test). (D) Correlation between $[^{68}\text{Ga}]\text{Ga-1}$ PET signal in tumors and tumor blood flow assessed by 3D-Doppler (percentage) in orthotopic SOJ6-xenografted mice ($n = 3$; two time points; Pearson correlation $R^2 = 0.751$; $*P = 0.0255$).

calorimetry (ITC) (Fig. 2C), which demonstrated the spontaneous formation of the $[^{69}\text{Ga}]\text{Ga-1}$ complex ($\Delta G = -6.99$ kcal/mol), resulting from the balanced and favorable contributions of both the enthalpic ($\Delta H = -4.05$ kcal/mol) and the entropic component ($-T\Delta S = -2.94$ kcal/mol). Finally, the molar ratio identified by the ITC-derived number of occupied sites ($n = 3.9$) (Fig. 2C) confirmed the 4:1 stoichiometry for each $[^{69}\text{Ga}]\text{Ga-1}$ complex as derived from the HRMS analysis described above. All of these results substantiate the practical and reliable synthesis of amphiphilic dendrimers bearing either free NOTA terminals or Ga^{3+} -chelated NOTA terminals.

Having the Ga^{3+} -chelated NOTA-terminating dendrimer $[^{69}\text{Ga}]\text{Ga-1}$ at hand, we studied its self-assembling properties. Although $[^{69}\text{Ga}]\text{Ga-1}$ is highly soluble in water (≥ 10 mg/mL), it self-assembles in water with a critical micelle concentration (CMC) of 64 ± 1 μM . We also assessed the octanol–water partition coefficient of $[^{69}\text{Ga}]\text{Ga-1}$ ($\log P$), with the P value being -140 ± 17 . This indicates that the $[^{69}\text{Ga}]\text{Ga-1}$ nanoparticles are hydrophilic, an advantageous feature for bioimaging. Dynamic light scattering (DLS) analysis also revealed that $[^{69}\text{Ga}]\text{Ga-1}$ formed small nanoparticles with average dimensions around 14 nm (Fig. 3A), a typical size for nanomicelles. The formed nanoparticles were stable and maintained similar size up to 1 wk (SI Appendix, Fig. S3). The effective formation of $[^{69}\text{Ga}]\text{Ga-1}$ nanomicelles was further confirmed by transmission electron microscopy (TEM) imaging, which showed small and spherical nanoparticles (Fig. 3B). We also examined the formation of $[^{69}\text{Ga}]\text{Ga-1}$ nanomicelles using atomistic molecular-dynamics (MD) simulations (24, 25). We observed that, during the timescale of the MD course (1.0 μs), the randomly distributed $[^{69}\text{Ga}]\text{Ga-1}$ complexes spontaneously aggregate into spherical micelles (Fig. 3C and D) with an effective average radius of 6.9 ± 0.2 nm. Accordingly, the corresponding

average $[^{69}\text{Ga}]\text{Ga-1}$ micelle diameter of 13.8 nm is in excellent agreement with the experimental value obtained from DLS and TEM (Fig. 3A and B). Further examination of the conformational structures of the formed nanomicelles (Fig. 3D) and the radial distribution of the terminal functions (Fig. 3E) revealed that the terminals bearing the Ga(III) functions are all located on the micellar periphery, and no backfolding was observed. Collectively, the structural and physicochemical properties exhibited by these self-assembled nanomicelles make them ideal candidates for nanotechnology-based imaging purposes, as presented below.

Radionuclide ^{68}Ga -Labeled Dendrimer Facilitates Excellent PET Imaging of Tumors. Motivated by the favorable self-assembling properties of $[^{69}\text{Ga}]\text{Ga-1}$, we prepared the corresponding radioactive dendrimer $[^{68}\text{Ga}]\text{Ga-1}$ for PET imaging. Using freshly generated $[^{68}\text{Ga}]\text{GaCl}_3$, the $[^{68}\text{Ga}]\text{Ga-1}$ complex was obtained with a radiochemical purity of $91.9 \pm 2.3\%$ soon after synthesis (SI Appendix, Fig. S4A). In addition, radiolabeling was stable up to 2 h after synthesis at room temperature and at 37°C , both in 0.9% NaCl solution and in human serum (SI Appendix, Fig. S4B). The $[^{68}\text{Ga}]\text{Ga-1}$ complex therefore satisfies the two important prerequisites for PET imaging, namely, high radiochemical purity and stability.

We then carried out PET imaging using the self-assembled nanomicelles of $[^{68}\text{Ga}]\text{Ga-1}$ to quantify their tumor targeting and uptake in various xenograft mouse models of cancer, including human prostate carcinoma (22Rv1 cell line; Fig. 4A), human glioblastoma (U87 cell line; Fig. 4B), human colorectal adenocarcinoma (HT-29 cell line; Fig. 4C), and human pancreatic adenocarcinoma (SOJ-6 cell line; Fig. 4D). In almost all cases, the observed effective tumor uptake and tumor-to-background ratios with $[^{68}\text{Ga}]\text{Ga-1}$ were superior to those obtained with $[^{18}\text{F}]\text{FDG}$,

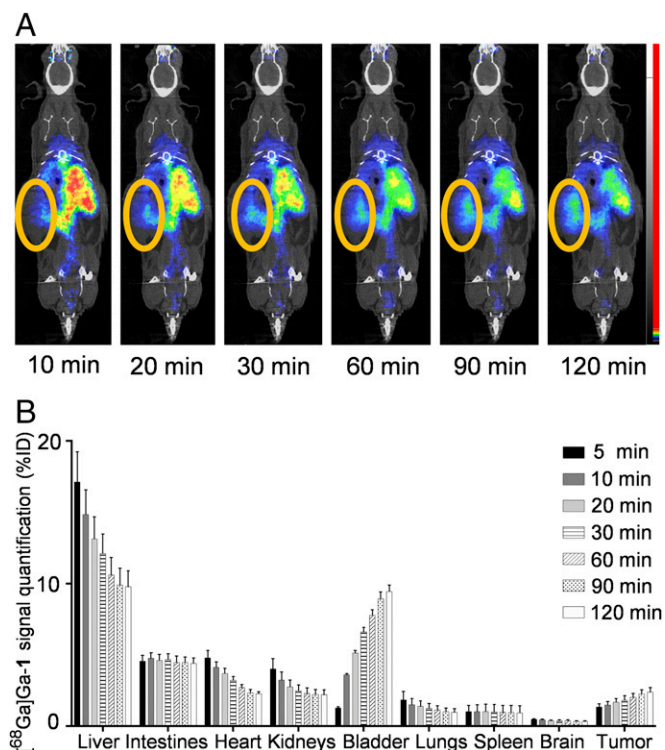


Fig. 6. The biodistribution and pharmacokinetics of $[^{68}\text{Ga}]\text{Ga-1}$ in the orthotopic xenograft mice using μPET dynamic acquisitions. (A) Representative images from PET imaging of $[^{68}\text{Ga}]\text{Ga-1}$ biodistribution in an orthotopic SOJ6-xenograft mouse 10, 20, 30, 60, 90, and 120 min after i.v. injection (fused PET and contrast-enhanced CT maximum intensity projections images). The orange ovals indicate tumor position. (B) Quantifications in organs from PET imaging of $[^{68}\text{Ga}]\text{Ga-1}$ biodistribution in mice 5, 10, 20, 30, 60, 90, and 120 min after i.v. injection. Organ uptakes are represented as mean \pm SD percentage injected dose for each organ and each time point (n = 3 mice).

the clinical gold reference for PET imaging in oncology (Fig. 4). $[^{18}\text{F}]\text{FDG}$ PET is based on the high consumption of glucose needed by the fast proliferating and nutrient-greedy cancer cells, and the major drawback of $[^{18}\text{F}]\text{FDG}$ is its physiological accumulation in tissues with high glucose consumption, like myocardium and brain (26), which increases the background signal and has a negative impact on the image quality. It should also be mentioned that certain tumors have low $[^{18}\text{F}]\text{FDG}$ uptake, including tumors derived from human glioblastoma U87 cells and human pancreatic adenocarcinoma SOJ-6 cells. Remarkably, our $[^{68}\text{Ga}]\text{Ga-1}$ nanoparticles had no preferential accumulation in the brain and a low uptake in the heart in all cases. Also, $[^{68}\text{Ga}]\text{Ga-1}$ successfully imaged tumors with both high and low $[^{18}\text{F}]\text{FDG}$ uptake, and the PET signal ratios were up to 14-fold higher with $[^{68}\text{Ga}]\text{Ga-1}$ nanoparticles than with $[^{18}\text{F}]\text{FDG}$ (Fig. 4). Therefore, we reasoned that the difference in $[^{18}\text{F}]\text{FDG}$ and $[^{68}\text{Ga}]\text{Ga-1}$ nanoparticle-based imaging could be ascribed to different tumor uptake mechanisms, with EPR-based tumor accumulation being the most plausible one for the uptake of $[^{68}\text{Ga}]\text{Ga-1}$.

EPR-Based Tumor Uptake of $[^{68}\text{Ga}]\text{Ga-1}$ for Effective PET Imaging. To investigate the uptake mechanism and obtain evidence for the EPR-based tumor accumulation of $[^{68}\text{Ga}]\text{Ga-1}$, we carried out a comparative study of PET imaging for tumor detection using the dendrimer nanosystem $[^{68}\text{Ga}]\text{Ga-1}$ and the small molecular complex $[^{68}\text{Ga}]\text{Ga-NOTA}$ (SI Appendix, Scheme S1A) in three pancreatic cancer models, namely, ectopic SOJ6- and LIPC-xenografted mice (Fig. 5A and B) and orthotopic SOJ6-xenografted

mice (Fig. 5C). $[^{18}\text{F}]\text{FDG}$ was used as the reference control in all studies. Coregistration with CT enabled precise, anatomical localization of PET signals for further quantification in tumors. The overall excellent tumor-to-background ratios highlighted the high quality of images and tumor targeting obtained with the $[^{68}\text{Ga}]\text{Ga-1}$ nanosystem. Indeed, the tumor uptake of the $[^{68}\text{Ga}]\text{Ga-1}$ nanoparticles was significantly higher than that of the simple $[^{68}\text{Ga}]\text{Ga-NOTA}$ complex and the clinical reference $[^{18}\text{F}]\text{FDG}$ (up to 100-fold increase) not only in the two ectopic pancreatic cancer mouse models (Fig. 5A and B) but also in the orthotopic pancreatic cancer model (Fig. 5C). Moreover, we observed a significant negative correlation between the tumor uptake of $[^{68}\text{Ga}]\text{Ga-1}$ and tumor blood flow as measured by 3D-Doppler (Fig. 5D). This suggests that $[^{68}\text{Ga}]\text{Ga-1}$ is more likely to accumulate in low-turbulent blood flow tumors, where the EPR effect contribution takes effect (27, 28). These results demonstrated that the significantly enhanced tumor uptake and the resulting superior imaging quality of $[^{68}\text{Ga}]\text{Ga-1}$ indeed stem from the nanoparticle-based EPR effect of the tumor microenvironment, which is distinctly different from the uptake mechanism of $[^{18}\text{F}]\text{FDG}$. The different uptake mechanisms of $[^{68}\text{Ga}]\text{Ga-1}$ and $[^{18}\text{F}]\text{FDG}$ mean that these two agents can be used in a complementary manner for tumor imaging, with $[^{68}\text{Ga}]\text{Ga-1}$ offering superior imaging, especially for the tumors that are otherwise undetectable using the clinical reference $[^{18}\text{F}]\text{FDG}$.

Advantageous Pharmacokinetics and Safety Profile of $[^{68}\text{Ga}]\text{Ga-1}$ for PET Imaging. Encouraged by these promising PET imaging results of $[^{68}\text{Ga}]\text{Ga-1}$, we further studied the pharmacokinetics and biodistribution of $[^{68}\text{Ga}]\text{Ga-1}$ in the orthotopic xenograft mice using μPET dynamic acquisitions (Fig. 6). This allowed us to trace and quantify the distribution of $[^{68}\text{Ga}]\text{Ga-1}$ across body organs from 5 min up to 2 h postinjection. Unlike drug delivery procedures, which require a constant supply of drug to the target tissue, bioimaging demands a rather rapid and intense accumulation of the imaging agent within tumor lesions and a fast clearance of the nonspecific, nonfixed radiotracer. By virtue of its distinct nanostructure, $[^{68}\text{Ga}]\text{Ga-1}$ has a biological elimination half-life of 171 ± 42 min, as obtained from pharmacokinetic analysis of $[^{68}\text{Ga}]\text{Ga-1}$ in blood samples (SI Appendix, Fig. S5). This biological half-life of $[^{68}\text{Ga}]\text{Ga-1}$ is particularly advantageous for PET imaging, as it allows effective image capture shortly after its administration (29, 30). This feature, coupled with the short physical half-life $[^{68}\text{Ga}]\text{Ga}$ (68 min), allows for both rapid and optimal imaging and fast elimination of radioactivity from the body. Further studies showed that the uptake of $[^{68}\text{Ga}]\text{Ga-1}$ in tumors was steadily increased, while that in the liver was significantly decreased within the 2-h imaging period (Fig. 6). This finding is also in line with the characteristic size and charge features of the $[^{68}\text{Ga}]\text{Ga-1}$ nanoparticles. Indeed, their nanosize allowed them to be readily trapped and enriched in the tumor via the EPR effect, and in the liver through the reticuloendothelial system, whereas their elimination was balanced between the kidneys and the intestines (Fig. 6). Collectively, the combination of high tumor signal stemming from the EPR effect, short biological half-life, and the absence of accumulation in most of the organs except the liver, all contribute to the favorable pharmacokinetic properties of the $[^{68}\text{Ga}]\text{Ga-1}$ nanoparticles for PET imaging of tumors.

It should be mentioned that, during the experimental period, the mice receiving $[^{68}\text{Ga}]\text{Ga-1}$ did not show any abnormal behavior or adverse effects. Healthy mice administered with $[^{68}\text{Ga}]\text{Ga-1}$ showed no cytokine induction, neither blood biochemistry defects nor organ damage, even when the administered dose of $[^{68}\text{Ga}]\text{Ga-1}$ was 10 times higher than the PET imaging dose (SI Appendix, Figs. S6–S8). These results confirm that $[^{68}\text{Ga}]\text{Ga-1}$ is devoid of toxic effects while delivering superior PET imaging quality.

Conclusions

In this work, we have established an effective and excellent self-assembling supramolecular dendrimer nanosystem capable of EPR-based tumor accumulation and PET imaging in various ectopic and orthotopic tumor-xenograft mouse models. Remarkably, the obtained PET images showed significantly higher quality in terms of sensitivity, specificity, and accuracy compared with the clinical reference [^{18}F]FDG and the small molecular [^{68}Ga]Ga-NOTA complex. Most importantly, this dendrimer system can detect imaging-refractory low-glucose-uptake tumors that are otherwise undetectable using [^{18}F]FDG. In addition, it is endowed with an excellent safety profile and favorable pharmacokinetics for PET imaging, highlighting its potential application for tumor imaging. It is also noteworthy that, until now, there has been no PET nanotracer currently available in oncology, although several have entered in clinical trials (31–33). It will be interesting to compare our dendrimer nanosystem with these reported PET nanotracers to further validate its imaging performance and potential for clinical translation. We will strive in our efforts in this direction.

It is important to note that the results reported in this study provide evidence that self-assembling dendrimer nanosystems hold promise as robust platforms for the delivery of agents in biomedical imaging. These nanosystems can potentially be extended to other imaging modalities such as single-photon emission computed tomography (SPECT) and magnetic resonance imaging (MRI) as well as to combined imaging–therapy applications such as those based on radiotherapy and imaging with the radionuclide [^{177}Lu]Lu. The possibility of closely controlling the chemistry, the size, and the hydrophobicity–hydrophilicity balance of amphiphilic dendrimers (7, 9, 34) provides us with a unique opportunity to fine-tune the self-assembling feature to create functional supramolecular nanosystems for on-demand delivery of different imaging and therapeutic agents

for a diverse range of imaging modalities and combined imaging–therapy applications (8, 35, 36). This will offer a particularly interesting perspective on the design and construction of tailor-made self-assembling dendrimer nanosystems for various biomedical applications in general.

Materials and Methods

A full description of the materials and methods is provided in the *SI Appendix*, including preparation and characterization of **1**, [^{69}Ga]Ga-1, [^{68}Ga]Ga-NOTA, and [^{68}Ga]Ga-1, as well as PET imaging of different xenograft mice along with the pharmacokinetics and toxicity evaluation. These include NMR, HRMS, TEM, DLS, CMC, ITC, computer modeling, radiolabeling, cell culture, animal xenograft, PET/CT imaging, biodistribution, blood biochemistry, immunotoxicity, and histopathological analysis. Additional figures include synthesis and characterization of **1** and [^{69}Ga]Ga-1 (*SI Appendix*, Figs. S1 and S2 and Scheme S1), nanoparticle stability, radiolabeling purity and stability of [^{68}Ga]Ga-1 (*SI Appendix*, Figs. S3 and S4), blood clearance (*SI Appendix*, Fig. S5), cytokine induction and serum biochemistry as well as histopathological analysis of main organs (*SI Appendix*, Figs. S6–S8) of mice treated with **1** and [^{69}Ga]Ga-1. All procedures involving animals were performed in accordance with protocols approved by the Institution's Animal Care and Use Committees at Aix-Marseille University or Peking University.

ACKNOWLEDGMENTS. We thank Advanced Accelerator Applications (Marseille) for [^{18}F]FDG, and Michel Skandalovski (Centre Européen de Recherche en Imagerie Médicale, Aix-Marseille University) and Marie Nollet (Centre de Recherche en Cardiovasculaire et Nutrition, Aix-Marseille University) for technical support. We are grateful to Fondation de l'Avenir, La Ligue Nationale Contre le Cancer (L.P. and Z.L.), EuroNanoMed II Grants ANR-15-ENM2-0006-02 and ANR-16-ENM2-0004-02 (to L.P.), Beijing Institute of Technology (Y.H.), Central Universities (Y.H.), Hunan Provincial Natural Science Foundation of China Grant 2018JJ1019 (to Y.H.), Huxiang Young Talent Program Grant 2018RS3094 (to Y.H.), and Italian Association for Cancer Research Grant IG17413 (to S.P.) for financial support. J.T., L.D., and W.L. are supported by the China Scholarship Council.

1. Chow EK-H, Ho D (2013) Cancer nanomedicine: From drug delivery to imaging. *Sci Transl Med* 5:216rv.
2. Li C (2014) A targeted approach to cancer imaging and therapy. *Nat Mater* 13:110–115.
3. Maeda H, Wu J, Sawa T, Matsumura Y, Hori K (2000) Tumor vascular permeability and the EPR effect in macromolecular therapeutics: A review. *J Control Release* 65:271–284.
4. Shi J, Kantoff PW, Wooster R, Farokhzad OC (2017) Cancer nanomedicine: Progress, challenges and opportunities. *Nat Rev Cancer* 17:20–37.
5. Chauhan VP, Jain RK (2013) Strategies for advancing cancer nanomedicine. *Nat Mater* 12:958–962.
6. Lehn J-M (2002) Toward self-organization and complex matter. *Science* 295:2400–2403.
7. Percec V, et al. (2010) Self-assembly of Janus dendrimers into uniform dendrimersomes and other complex architectures. *Science* 328:1009–1014.
8. Wei T, et al. (2015) Anticancer drug nanomicelles formed by self-assembling amphiphilic dendrimer to combat cancer drug resistance. *Proc Natl Acad Sci USA* 112:2978–2983.
9. Sherman SE, Xiao Q, Percec V (2017) Mimicking complex biological membranes and their programmable glycan ligands with dendrimersomes and glycodendrimersomes. *Chem Rev* 117:6538–6631.
10. Liu X, et al. (2014) Adaptive amphiphilic dendrimer-based nanoassemblies as robust and versatile siRNA delivery systems. *Angew Chem Int Ed Engl* 53:11822–11827.
11. Chen C, et al. (2016) Mastering dendrimer self-assembly for efficient siRNA delivery: From conceptual design to in vivo efficient gene silencing. *Small* 12:3667–3676.
12. Gambhir SS (2002) Molecular imaging of cancer with positron emission tomography. *Nat Rev Cancer* 2:683–693.
13. James ML, Gambhir SS (2012) A molecular imaging primer: Modalities, imaging agents, and applications. *Physiol Rev* 92:897–965.
14. Beyer T, Townsend DW, Czernin J, Freudenberg LS (2011) The future of hybrid imaging—part 2: PET/CT. *Insights Imaging* 2:225–234.
15. Cutler CS, Hennkens HM, Sisay N, Huclier-Markai S, Jurisson SS (2013) Radiometals for combined imaging and therapy. *Chem Rev* 113:858–883.
16. Wadas TJ, Wong EH, Weisman GR, Anderson CJ (2010) Coordinating radiometals of copper, gallium, indium, yttrium, and zirconium for PET and SPECT imaging of disease. *Chem Rev* 110:2858–2902.
17. Bartholomä MD (2012) Recent developments in the design of bifunctional chelators for metal-based radiopharmaceuticals used in positron emission tomography. *Inorg Chim Acta* 389:36–51.
18. Price EW, Orvig C (2014) Matching chelators to radiometals for radiopharmaceuticals. *Chem Soc Rev* 43:260–290.
19. Kumar P, Tripathi S, Mehta N, Wickstrom E, Thakur M (2017) A preclinical evaluation of Ga-68 labeled NODAGA and DOTA peptide conjugates to image breast cancer. *J Nucl Med* 58:675.
20. Zhou Z, et al. (2018) Negative dendritic effect on enzymatic hydrolysis of dendrimer conjugates. *Chem Commun (Camb)* 54:5956–5959.
21. Liu X, et al. (2015) Promoting siRNA delivery via enhanced cellular uptake using an arginine-decorated amphiphilic dendrimer. *Nanoscale* 7:3867–3875.
22. Yu T, et al. (2012) An amphiphilic dendrimer for effective delivery of small interfering RNA and gene silencing in vitro and in vivo. *Angew Chem Int Ed Engl* 51:8478–8484.
23. Brevard C, Granger P (1981) *Handbook of High Resolution Multinuclear NMR* (Wiley, New York), pp 132–133.
24. Bogusz S, Venable RM, Pastor RW (2000) Molecular dynamics simulations of octyl glucoside micelles: Structural properties. *J Phys Chem B* 104:5462–5470.
25. Thornalley KA, Laurini E, Pridl S, Smith DK (2018) Enantiomeric and diastereomeric self-assembled multivalent nanostructures: Understanding the effects of chirality on binding to polyanionic heparin and DNA. *Angew Chem Int Ed Engl* 57:8530–8534.
26. Kato T, Inui Y, Nakamura A, Ito K (2016) Brain fluorodeoxyglucose (FDG) PET in dementia. *Ageing Res Rev* 30:73–84.
27. Kim E, Kim J, Maelandsmo GM, Johansen B, Moestue SA (2017) Anti-angiogenic therapy affects the relationship between tumor vascular structure and function: A correlation study between micro-computed tomography angiography and dynamic contrast enhanced MRI. *Magn Reson Med* 78:1513–1522.
28. Viillard C, Larrivé B (2017) Tumor angiogenesis and vascular normalization: Alternative therapeutic targets. *Angiogenesis* 20:409–426.
29. Hansen AE, et al. (2015) Positron emission tomography based elucidation of the enhanced permeability and retention effect in dogs with cancer using copper-64 liposomes. *ACS Nano* 9:6985–6995.
30. Ni D, et al. (2018) Radiolabeled polyoxometalate clusters: Kidney dysfunction evaluation and tumor diagnosis by positron emission tomography imaging. *Biomaterials* 171:144–152.
31. Lee H, et al. (2017) ^{64}Cu -MM-302 positron emission tomography quantifies variability of enhanced permeability and retention of nanoparticles in relation to treatment response in patients with metastatic breast cancer. *Clin Cancer Res* 23:4190–4202.
32. Pan Y, et al. (2014) Endoscopic molecular imaging of human bladder cancer using a CD47 antibody. *Sci Transl Med* 6:260ra148.
33. Schluep T, et al. (2009) Pharmacokinetics and tumor dynamics of the nanoparticle IT-101 from PET imaging and tumor histological measurements. *Proc Natl Acad Sci USA* 106:11394–11399.
34. Schenning AP, et al. (1998) Amphiphilic dendrimers as building blocks in supramolecular assemblies. *J Am Chem Soc* 120:8199–8208.
35. Filippi M, et al. (2014) Dendrimersomes: A new vesicular nano-platform for MR-molecular imaging applications. *Chem Commun (Camb)* 50:3453–3456.
36. Filippi M, et al. (2015) Novel stable dendrimersome formulation for safe bioimaging applications. *Nanoscale* 7:12943–12954.